Scientific Reports

https://doi.org/10.1038/s41598-026-59604-6

Article in Press

A Hybrid Reconstruction Approach for Estimating Topside Ionospheric Scale Height and Its Altitudinal Variation Using Jicamarca ISR Measurements

Received: 16 December 2025

Accepted: 22 June 2026

Published online: 01 July 2026

Cite this article as: Guru K.S.K., Sripathi S., Singh R. *et al.* A Hybrid Reconstruction Approach for Estimating Topside Ionospheric Scale Height and Its Altitudinal Variation Using Jicamarca ISR Measurements. *Sci Rep* (2026). https://doi.org/10.1038/s41598-026-59604-6

K. Siba Kiran Guru, S. Sripathi, Ram Singh, Rajesh Kumar Barad, Danny Scipion & A. P. Dimri

A Hybrid Reconstruction Approach for Estimating Topside Ionospheric Scale Height and Its Altitudinal Variation Using Jicamarca ISR Measurements

K Siba Kiran Guru[1,*], S Sripathi[1], Ram Singh[3], Rajesh Kumar Barad[4], Danny Scipion[3], and A.P. Dimri[2]

[1]Equatorial Geophysical Research Laboratory (EGRL), Indian Institute of Geomagnetism (IIG), Krishnapuram, Tirunelveli-627011, Tamil Nadu, India
[2]Indian Institute of Geomagnetism, Plot-5, Sector-18, New Panvel, Navi Mumbai, 410218, India
[3]Jicamarca Radio Observatory (ROJ), Geophysical Institute of Peru (IGP), Lima, Peru
[4]Paris City University, Paris Institute of Global Physics (IPGP), CNRS UMR 7154, Paris, France
[*]*sibakiranguru@gmail.com*

ABSTRACT

In ionospheric research, accurately representing the topside electron density profile is essential for predicting radio wave propagation and mitigating ionospheric effects on communication and navigation systems. Despite advances in global models and satellite observations, region-specific and continuous modelling of the topside ionosphere remains challenging due to limited in-situ measurements. Reliable reconstruction of the topside ionosphere using empirical formulations requires precise knowledge of the scale height at the F_2 peak (H_0) and its linear altitudinal variation (α), especially over the electrodynamically complex equatorial and low-latitude regions. In this study, 13 years (2013-2024) of incoherent scatter radar measurements from the Jicamarca Radio Observatory, Peru, a prominent dip-equatorial station, are utilized to extract realistic topside parameters. A *Hybrid reconstruction strategy* is employed to adaptively select best suitable formulation between the α-Chapman and semi-Epstein formulations at each time step using fitting error metrics derived from least-square optimization. This approach enables simultaneous and physically consistent estimation of H_0 and α.The results revealed pronounced diurnal, seasonal, and solar-geomagnetic variability in the topside parameters. Overall, this analysis demonstrate the effectiveness of Hybrid approach in improving the topside electron density reconstruction, and the insights gained may be integrated with existing models to enhance their regional accuracy.

Introduction

The ionosphere, a crucial region of Earth's upper atmosphere extending from $\sim$ 50 to 1000 km in altitude, plays a key role in various space weather phenomena. Due to significant variation in its plasma composition and electron density under varied space weather conditions, the propagation of radio waves, particularly in the high-frequency (HF) and very-high-frequency (VHF) bands are impacted, thereby affecting communication, navigation and surveillance systems. Consequently, understanding the vertical structure and temporal variability of ionospheric electron density is essential, especially over the equatorial and low-latitude regions where complex electrodynamics make ionospheric processes more variable and often unpredictable. Based on altitude-dependent ionization and recombination processes, the ionosphere is conventionally categorized into the D, E and F layers[1]. The F-layer is further divided into F_1 and F_2 layers, with the latter receiving greater attention in ionospheric research, as it hosts peak electron density (N_mF_2) at corresponding peak height (h_mF_2)[2]. Further, the F_2 layer exhibits pronounced spatial and temporal variability driven by solar extreme ultraviolet (EUV) radiation, geomagnetic activity, thermospheric winds, and electrodynamic $\vec{\boldsymbol{E}} \times \vec{\boldsymbol{B}}$ drifts, making it highly sensitive to both regular and disturbed space weather conditions[1,2].

To investigate ionospheric structure and dynamics, researchers employ a variety of ground and space-based observational techniques. Ionosondes, are among the oldest and most widely used ground-based instruments, providing vertical sounding of the ionosphere by transmitting radio pulses and analysing their reflected echoes[3]. Although ionosondes effectively characterize the bottomside ionosphere (below F_2 peak), they are inherently limited in probing the topside ionosphere (above F_2 peak), where a major fraction of the ionosphere's total electron content (TEC) resides[4,5]. The electrodynamics of topside also differs markedly from bottomside, as there is negligible local ion production at higher altitudes. Moreover, in the topside ionosphere, a smooth transition occurs from heavier O^+ ions to lighter H^+ and He^+ ions, leading to a gradual and monotonic decrease

in electron density[1]. Space-based platforms such as satellites and sounding rockets equipped with Langmuir probes (LP)[6–8] provide valuable in-situ measurements of the topside ionosphere, but their spatial and temporal coverage is often constrained by limited revisit times over specific ground locations. In addition, satellite-based radio occultation (RO) techniques provide complementary electron density profiles (EDPs) with global coverage, though with relatively lower vertical resolution and sparse temporal sampling over any particular region[9,10]. In this context, incoherent scatter radars (ISRs) serve as one of the most powerful ground-based tools for comprehensive vertical ionospheric profiling[11,12]. ISRs, transmit high-power radio waves that are weakly scattered by thermal fluctuations of the free electrons in the ionosphere. By analysing the backscattered spectrum, ISRs can simultaneously determine a range of plasma parameters, including electron density (N_e), ion and electron temperatures (T_i and T_e), ion composition, and drift velocity. They provide altitude resolved measurements from the E region to well into the topside F region and beyond, with high temporal resolution and accuracy[13,14]. Despite their superior capabilities, ISR observations face challenges, particularly under conditions of low signal-to-noise ratio (SNR) in the topside ionosphere, where the N_e is low and backscatter power is very weak[15]. Furthermore, due to the requirement of large infrastructure and operational costs, only a few ISR facilities operating worldwide (e.g., *Jicamarca*, *Millstone Hill*, and *EISCAT*), restricting their global applicability in wide range of ionospheric research.

To overcome these challenges, numerous empirical functions and models have been employed to reconstruct topside EDPs. Empirical models such as the International Reference Ionosphere (IRI)[5,16], NeQuick[17], and physics-based models such as SAMI2[18], which simulates the ionospheric dynamics along magnetic field lines, are widely used to represent the vertical electron density structure under varying geophysical conditions[19–23]. These models often employ analytical formulations based on physical parameters to describe the electron density. Among these, the α-Chapman function is most commonly used for representing the ionosphere, particularly the F region, as it is based on theoretical considerations of photoionization and recombination under an isothermal atmosphere[4,24–27]. In recent years, the semi-Epstein formulation has gained increasing attention due to its flexibility in reproducing realistic ionospheric conditions through adjustable parameters[16,28–31]. Additionally, previous studies have shown that during disturbed ionospheric conditions, such as geomagnetic storms, the Epstein formulation better describes the ionospheric density distribution than the Chapman method[32].

In all mathematical formulations used in ionospheric modelling, the scale height (H) is a fundamental parameter that governs the shape of the topside EDP and characterizes the rate at which the electron density decay with altitude. In the context of ionospheric studies, three main definitions of scale height are commonly used[11,25]: **(a) Vertical Scale Height**, defined as $VSH = \left(-\frac{1}{N_e}\frac{\partial N_e}{\partial z}\right)^{-1}$, which represents the local density gradient scale height at a given altitude and in general practice, it is often evaluated near the F_2 peak; **(b) Plasma Scale Height**, given by $H_p = \frac{k_\beta T_p}{m_i g}$, where k_β is the Boltzmann constant, T_p is the plasma temperature, m_i is the ion mass, and g is the gravitational acceleration; and **(c) Effective Scale Height** (H_m), obtained by fitting analytical formulations to observed electron density profiles (EDPs). Since direct estimation of H_p variation with altitude at a given location is not feasible, effective scale heights are generally used for the reconstruction of EDPs. Under conditions of diffusive equilibrium, the VSH can be theoretically equalised with H_p[1,33], but in actual scenario the ratio between the two varies significantly[12]. The scale height varies both temporally and spatially in response to solar and geomagnetic forcing. For simplicity, a fixed scale height approach has been widely used in past studies to model the topside EDP[4,25,26,34,35]. However, subsequent investigations revealed that this assumption cannot adequately represent the actual ionospheric behaviour, as the scale height tends to vary linearly within a few hundred kilometres above the F_2 peak[27,31,33,36–38], and exhibits a higher order variation at much greater altitudes[39], as reported in recent studies. Therefore, accurate estimation of the scale height and its altitudinal variation is essential for understanding the thermal structure and plasma dynamics of the topside ionosphere, and for improving the reliability of empirical models and radio propagation predictions. Earlier studies on scale height estimation using the Chapman formulation have shown that the corresponding scale height representation may exhibit limitations near the F_2 peak transition region and can become mathematically discontinuous[4]. In most previous investigations, such limitations were generally addressed by excluding the transition region close to the F_2 peak during topside scale height estimation. However, the capability of the two widely used analytical formulations, namely the α-Chapman and semi-Epstein functions, to reproduce the complete vertical EDP and the corresponding scale height variation under varying solar-geomagnetic conditions has not been explored in detail. This constitutes one of the key motivations behind the present study.

The primary objective of this study is to reconstruct vertical EDPs over the magnetic equator using ISR electron density observations from the Jicamarca Radio Observatory (JRO), covering the period 2013 to 2024 and encompassing a wide range of solar activity conditions. The JRO (Geog: 11.95° S, 76.87° W; Geom: 0.6° N) is a dip-equatorial station located near Lima, Peru, and hosts one of the world's most powerful and sophisticated ISR systems[40,41], providing a unique platform for investigating equatorial and low-latitude ionospheric dynamics. In this work, instead of relying on a single analytical formulation

as conventionally done in earlier studies[11,12,38], an adaptive Hybrid reconstruction approach is employed. In this framework the best suitable reconstruction method among the α-Chapman and semi-Epstein formulations is dynamically selected at each time step under varied solar-geomagnetic conditions, based on realistic fitting performance of observed EDPs. This strategy enables more accurate estimation of key topside parameters such as the scale height at the F_2 peak (H_0) and its linear altitudinal gradient (α). The time-dependent Hybrid reconstruction strategy employed in this study is explained in detail in subsequent sections. Furthermore, this study investigates the seasonal, solar activity, and geomagnetic activity–dependent variations of these derived topside parameters to better understand their physical behaviour under varied solar and geomagnetic conditions. Due to limited in-situ measurements and inherent uncertainties in global empirical models, ISR-based observations remain invaluable for directly examining the topside ionospheric structure and validating model-derived parameters. Insights gained from this study can ultimately be integrated with bottomside ionosonde data from other locations to reconstruct near-accurate topside profiles in regions lacking ISR coverage, thereby enhancing the reliability of global ionospheric models for space weather applications.

Results and Discussion

This section highlights the key results obtained from the study, which are organized into two main parts. The first part focuses on the motivation behind establishing the time-dependent Hybrid reconstruction approach by combining two widely used traditional methods namely, **(a)** α-Chapman and **(b)** Semi-Epstein formulations rather than using them individually, and evaluates its performance in reproducing the observed ISR derived EDPs under varied solar and geomagnetic conditions. The second part presents a detailed analysis of the extracted topside scale height and its linear altitudinal gradient, highlighting their diurnal, solar, and geomagnetic dependencies, along with seasonal variability.

Need for a Hybrid Reconstruction Approach and Its Importance

The profile-fitting procedure employed in this study is demonstrated with three representative examples of ISR-JRO derived EDPs and their corresponding Chapman and Epstein fits, as shown in **Panel A** of **Figure 1** [1]. **Figure 1A(a-c)** corresponds to three different local time (LT) instances at 00:35, 08:45, and 17:15 LT on a typical day, 21 March 2024, illustrating the differences between both modelling approaches in representing the actual ionospheric density during distinct time periods. During the fitting procedure, the peak parameters were not strictly constrained, allowing both formulations to flexibly adjust the complete profile shape and to obtain the optimum least-square reconstruction of the observed EDP. In each subpanel, the solid black dots represent the actual ISR electron densities, while the blue and pink dashed curves represent the respective least-square fitted Chapman and Epstein profiles with constant H_0, as indicated in the legends. The solid pink and blue curves correspond to the topside fits using linearly varying scale height, with their associated α values also shown in the legends. The complete procedure of profile fitting and extraction of topside ionospheric parameters is explained in details in the ***Methods Section***.

From **subpanel (a)** of **panel 1A**, it can be observed that the α-Chapman function effectively reproduces the observed electron density curvature during the nighttime. However, as shown in **subpanels (b)** and **(c)** of **panel 1A**, the Chapman function fails to accurately represent the measured daytime and evening density profiles, particularly underestimating the peak electron density. In contrast, the semi-Epstein formulation performs better during the daytime and evening sectors, successfully reproducing the observed EDPs. This demonstrates a clear discrepancy in the performance of the two models under different LT sectors. A recent study over the Indian sector also highlights the superior performance of semi-Epstein approach in reconstructing topside EDPs using a linearly varying topside scale height[31]. Although this study did not exclusively examine the diurnal, seasonal and geomagnetic variability of topside scale-height gradient, it emphasized the critical role of accurately estimating the topside scale height gradient for reliable reconstruction of vertical EDPs.

Furthermore, the α values retrieved by both methods differ by nearly an order of magnitude among the three cases presented. **Subpanel (b)** of **panel 1A** shows that during the daytime both models yield negative α values, with the Epstein-derived gradient being smaller in magnitude than the Chapman-derived one. In contrast, **subpanels (a)** and **(c)** of **panel 1A** show small positive and negative gradients, respectively, corresponding to the nighttime and evening periods. These observations are consistent with earlier studies on topside scale height gradients, though the magnitude of the negative gradient observed here differs slightly from previous reports that relied solely on the Chapman function[38].

To provide a clearer picture of the model discrepancies, **Panel B** of **Figure 1** presents the Range-Time-Density (RTD) maps of the observed and modelled electron densities for the same day, 21 March 2024. All profiles were binned into 15-minute intervals and 5 km height resolution, with the corresponding electron density or residuals shown in the respective colour scales. The observed and fitted h_mF_2 values are overlaid on the respective RTD maps as black curves in **subpanels (a-d)** of **panel 1B**. **Subpanel 1B(a)** shows the actual ISR-measured densities, while **subpanels 1B(b-d)** represent the fitted densities obtained from

the α-Chapman, semi-Epstein, and Hybrid reconstruction approaches, respectively. The corresponding differences between observed and modelled densities are depicted as residual maps in **subpanels 1B(e-g)**. From the residual maps it is evident that the Chapman formulation exhibits significant daytime errors, particularly between 07:00-17:00 LT, where it underestimates the actual density (highlighted by red circle in **subpanel 1B(e)**). The semi-Epstein model reduces these discrepancies, especially in the daytime sector, though small overestimation errors persist in the early morning and evening hours in the bottomside region (as indicated by the two small red circles on **subpanel (f)**). In contrast, as seen in **subpanel (g)** of **panel 1B** that the time-dependent Hybrid reconstruction approach substantially minimizes residuals across all LT sectors, providing much better agreement with the measured ISR densities. Overall, this adaptive Hybrid reconstruction strategy enables a more realistic reconstruction of the EDPs by dynamically selecting the most suitable formulation under varying ionospheric conditions while minimizing the limitations of individual analytical approaches. Using different datasets previous studies on topside ionosphere have also highlighted the varying performance of analytical formulations in reproducing the actual ionospheric conditions and emphasized the need for more flexible approaches by use of multiple formulations with variable topside scale height for improved modelling under diverse geophysical conditions[32,42,43]. The present study aligns with these concepts by implementing a time-dependent model selection framework to improve the ionospheric modelling under varied solar geomagnetic conditions.

Motivated by the model discrepancies discussed earlier, all available ISR-JRO derived EDPs between 2013-2024 (after applying the quality-control and filtering criteria described in ***Methods Section***) were considered for the Hybrid analysis. The statistical distribution of the considered profiles (a total of **19,201**) is presented in **Figure 2 (a-c)** [2] with respect to LT, solar activity (*F10.7*, with a threshold of 120 sfu to distinguish between moderate and high conditions), and geomagnetic activity (K_p, with a threshold of 2 to distinguish between low and high conditions). Each classification in the bar plots is represented by distinct colours and the corresponding number of profiles in each category is also indicated in the legends, demonstrating the dataset considered is well distributed across these conditions. The relatively low threshold $K_p \geq 2$ was adopted to ensure uniform statistical representation across geomagnetic conditions, as higher thresholds resulted in limited data coverage. A similar classification has been employed in previous ISR-JRO based studies[38].

Further, for all the considered profiles, error analysis was performed by computing the Root Mean Square Error (*RMSE*) and Normalized Root Mean Square Error (*nRMSE*) for each fitted profile using Chapman, semi-Epstein and Hybrid reconstruction approach (refer ***Methods Section***). In this context, the *RMSE* represents the height-integrated deviation between the reconstructed and observed EDPs, while the *nRMSE* is the normalized form of *RMSE* with respect to the observed N_mF_2. Thus, these two parameters serve as key indicators of the robustness and fitting accuracy of the respective reconstruction models across varying ionospheric conditions[22,44]. **Figure 3(a-d)** [3] presents the comparison of *RMSE* and *nRMSE* for the three methods under varying solar (**panels 3a** and **3b**) and geomagnetic (**panels 3c** and **3d**) activity conditions. To determine these error factors, all profiles were binned into 15-minute temporal and 5 km height resolutions. The blue, green, and orange curves correspond to the Chapman, semi-Epstein, and Hybrid reconstruction methods, respectively, with solid and dashed lines representing high and low geomagnetic activity levels (for K_p) and high and moderate solar activity levels (for *F10.7*). For better visualization of *nRMSE* variation during daytime, it is highlighted with a violet patch in **panels 3c** and **3d**.

It is evident from the figure that the Hybrid reconstruction method employed in this study consistently exhibits the lowest *RMSE* and *nRMSE* values across all conditions, confirming its superiority over traditional single analytical formulation-based profile reconstruction and modelling approaches in representing the actual ionospheric conditions, particularly the F-region over the equator. The Chapman model performs relatively better during early morning and nighttime hours, where the topside density varies more gradually; however, it produces high errors in day time (especially, during 09:00 – 16:00 LT), due to its limited capability in capturing steep density and scale height gradients. In contrast, the semi-Epstein formulation perform better during the daytime, effectively capturing the topside variability but still showing relatively larger errors during nighttime. From the highlighted *nRMSE* regions of **panel 3c** and **3d**, it can be clearly seen that during daytime the Hybrid reconstruction approach reduces the error to below 5%, whereas the Chapman model alone shows errors up to 9%. Similarly, during nighttime, the Hybrid reconstruction method maintains the errors below 8%, while the Epstein model alone exhibit errors exceeding 12%. Notably, even during the highly dynamic Pre-Reversal Enhancement (PRE) and post-midnight periods where rapid variations in vertical plasma drift make reconstruction of EDPs a highly challenging task when traditional methods are applied individually, the Hybrid reconstruction approach continues to perform robustly, maintaining lower residual errors. These findings underscore that the Hybrid reconstruction approach provides more accurate and reliable representations of topside electron density, particularly in terms of scale height and gradient parameters, under dynamic geophysical conditions.

Analysis of Topside Scale Height and Its Gradient

This section presents a comprehensive analysis of the topside scale height (H_0) and its linear gradient (α), estimated using the Hybrid EDP reconstruction method. The results provide new insights into the diurnal, seasonal, solar, and geomagnetic variability of these parameters over the electrodynamically intricate equatorial region.

Diurnal Variation of H_0 and α under different solar and geomagnetic conditions

The Hybrid reconstruction method (***Methods Section***) was applied to estimate the primary topside ionospheric parameters N_mF_2, h_mF_2, H_0 and α from all the considered ISR-JRO profiles. The analysis was carried out by averaging these parameters into 15-minute time bins to capture their diurnal evolution more precisely. The colour scheme representing different solar and geomagnetic conditions remains consistent across all figures (***Figures 4, 5, S1*** and ***S2***): pink and green correspond to high and moderate *F10.7* levels, respectively, while yellow and blue denote high and low K_p conditions. Standard deviation bars indicate the variability within each 15-minute interval. For a deeper analysis, all the considered EDPs were categorized into three seasons based on observation months to examine the seasonal trends in topside parameters under varying solar and geomagnetic activity levels:

(a) December Solstice (southern summer): November, December, January, and February

(a) June Solstice (southern winter): May, June, July, and August

(a) Equinox: March, April, September, and October

Before focusing on the scale height variation, the diurnal behavior of N_mF_2 and h_mF_2 is summarized in ***Figure S1*** (Supplementary Material). Both parameters exhibit expected diurnal trends with higher peak during elevated solar flux and geomagnetic activity, consistent with earlier studies[11,20]. The N_mF_2 (**panels S1(a-b)**) displays a distinct daytime enhancement and night time reduction under all activity conditions, with an exception observed during moderate solar flux conditions, where the night time density became comparable to daytime level. However, such post-midnight increments in the ionospheric density have been well reported in previous studies and are generally attributed to factors such as equatorward neutral winds, penetration electric fields, and downward plasma diffusion from the plasmasphere[45–47]. The h_mF_2, on the other hand shows a clear predawn minimum, followed by a steady daytime increase, and a pronounced maximum around PRE-period, before a sharp decline in nighttime. Interestingly, under moderate solar flux conditions, a distinct early morning peak in h_mF_2 is also noticeable around 4:00 - 6:00 LT, which could be linked to upward drift associated with enhanced electric fields near the dawn sector[48,49]. Seasonal analysis revealed that these two distinct features, namely the post-midnight density enhancement and early morning h_mF_2 peak are more prominent during the Equinox season (not shown here). As discussed, the N_mF_2 and h_mF_2 values obtained through the Hybrid reconstruction approach follow the expected diurnal and seasonal characteristics, indicating that the time-based adaptive model selection approach employed in this study preserves the physical consistency of the ionospheric parameters.

In a similar manner, the diurnal variation of H_0 and α derived using Hybrid reconstruction approach under varied solar and geomagnetic conditions are presented in **Figure 4(a-d)** [4]. **Panels 4a** and **4b** illustrates the variation of H_0 with respect to *F10.7* solar flux and K_p index, respectively, while **panels 4c** and **4d** depict the corresponding behavior of α. As in the previous analyses, the data were averaged into 15-minute bins, and the vertical bars indicate the standard deviation within each bin. A clear diurnal pattern is evident in the scale height, showing an early-morning peak around 04:00 - 06:00 LT, followed by a descent to a minimum near 07:00 - 08:00 LT, then a pronounced maximum near noon time, and a gradual decline during nighttime. The early morning peak in H_0 closely resembles enhancement in h_mF_2 noted in **Figure S1**. The scale height values are consistently larger during high solar activity compared to moderate conditions as shown in **panel 4a**. This can be attributed to enhanced solar EUV radiation during periods of high solar flux, which increases the thermospheric and electron temperatures. As a result, the ionosphere-plasmasphere region expands, leading to an enhanced O^+ density[50]. Since, the plasma scale height (H_p) is directly proportional to temperature, higher EUV flux leads to larger H_p, eventually increasing the effective H_0. In contrast, the geomagnetic activity (K_p) appears to have a smaller influence on the mean diurnal variation of H_0 (as shown in **panel 4b**). Particularly, during the morning hours up to 10:00 LT, there is no pronounced difference between low and high geomagnetic conditions, with only a slight divergence around noon. Several previous studies have also reported a strong positive correlation between h_mF_2 and H_0[51,52]. Our analysis confirms this relationship across different solar and geomagnetic conditions, showing a high degree of correlation (not shown here). Notably, the observed diurnal variation of H_0 is in good agreement with independent estimates derived from radio occultation profiles reported in previous studies[53], further supporting the reliability of the proposed Hybrid EDP reconstruction strategy. A similar consistency is also observed in the diurnal variation of α, which is analogous to the gradient parameter (g) used in NeQuick model, testifying that the observed features are robust across different datasets and methodologies.

Now, turning to the mean diurnal variation of α, distinct features emerges under varied solar and geomagnetic conditions. As highlighted by the grey dotted box in **panel 4c**, during moderate solar flux conditions, α exhibits a prominent early-morning peak (04:00 - 06:00 LT), indicating a sharp increase in the topside scale height during this period. This enhancement can be attribute to the well-known morning overshoot of electron temperature (T_e), which is particularly strong near dip-equator[13,54,55]. The increase in T_e elevates the H_p, thereby increasing α temporarily. After sunrise, as ionization intensifies, the enhanced cooling rate due to collision with neutrals causes the temperature and consequently α to decline. During daytime hours (09:00 - 14:00 LT), the mean α assumes slightly negative values, suggesting a gradual decrease in the topside scale height with altitude. However, this negative gradient is considerably smaller than that reported in earlier studies using the Chapman function alone, where a much stronger negative α was observed during daytime based on O^+ density alone[38]. In contrast, the present study utilizes the electron density, which includes contributions from lighter ion species such as H^+, He^+ and other minor species at higher altitudes, resulting in a gradual variation of the topside scale height during daytime, thereby representing a realistic topside ionospheric condition.

Under high solar activity, the early-morning peak in α becomes less pronounced, and the mean gradient remains near-neutral or slightly positive, implying a relatively steady increase in topside scale height with altitude. This behavior of α is consistent with the known inverse relationship between the morning T_e overshoot and solar activity, wherein the overshoot weakens under high solar activity conditions[54], thereby manifesting strong physical relation between topside scale height variations and underlying ionospheric dynamics. A particular noteworthy feature revealed in this study is the nighttime enhancement in α around 20:00 LT, marked by pink dotted box in **panel 4c**, indicating a sharp nighttime enhancement in the topside scale height. This feature has not been widely reported in earlier studies. It can be associated with anomalous nighttime increase in T_e observed in recent Jicamarca ISR studies[56]. The potential drivers behind this higher-altitude heating may include plasma transport processes, reduced cooling rates, and enhanced upward drifts near the dusk sector. Previous studies have also demonstrated possible links between vertical $\vec{E} \times \vec{B}$ drifts and the topside parameters H_0 and α using model simulations such as SAMI2[25,38]. In the present work no model-based analysis was performed, as the primary objective was to assess the performance and necessity of the Hybrid EDP reconstruction approach using actual ISR observations. Moreover, direct drift measurements were not available for these intervals, since ISR-JRO operates either in drift or density mode at a time, preventing their simultaneous observations.

Previous investigations have also noted a negative correlation between N_mF_2 and α[51,52]. However, our analysis indicates only a weak negative correlation between these two parameters (not shown here), implying that density variation near to F_2 peak plays a relatively minor role in controlling topside scale height variability. Instead the topside is more sensitive to temperature and electrodynamic vertical transport processes, which primarily modify the plasma distribution above the peak rather than the peak density itself. Recent studies using Swarm satellite observations also indicate a similar climatology between α and T_e[33], further validating the temperature dependence of α. The variation of α with respect to K_p, shown in **panel 4d**, exhibits broadly similar characteristics. Notably, the early-morning and evening enhancements in α are more prominent under low geomagnetic activity, suggesting that quiet-time conditions favour stronger topside heating and expansion compared to disturbed periods.

Further, **Figure 5** [5] illustrates the seasonal variation in the diurnal behaviour of the H_0 (**panels 5(a-c)**) and α (**panels 5(d-f)**) under high and moderate solar activity conditions. The early-morning peak in H_0 is evident during December Solstice and Equinox, but notably absent in June Solstice. Interestingly, under moderate solar activity during December Solstice, the morning peak in H_0 surpasses the noon peak (highlighted by the black dotted box), suggesting the influence of dynamic early morning processes and the prominent role of electrodynamic $\vec{E} \times \vec{B}$ drift[49]. Overall, the scale height remains lower during June Solstice compared to December Solstice and Equinox, reflecting seasonal differences in thermospheric temperature and compositions. The gradient α also exhibits a clear seasonal dependence as well. Under moderate solar activity, a larger negative gradient is seen during the daytime in December Solstice, indicating a steeper decrease of topside scale height with altitude. Evening enhancements in α are a consistent feature across all seasons under high solar activity, with the peak occurring earlier in June Solstice and more prominently in December Solstice. Additionally, a pronounced daytime enhancement in α is particularly evident during Equinox months. **Figure S2** (supplementary material) shows that the seasonal patterns in H_0 and α for varying K_p conditions remain largely consistent with those observed under different solar activity levels, with only minor differences. The influence of geomagnetic activity is relatively weak during Equinox but becomes slightly more pronounced during December and June Solstice, especially around noon and post-sunset hours. Interestingly, under low geomagnetic activity, the early-morning peak in H_0 is present during June Solstice, suggesting quiet-time conditions may favour localized topside expansion even in relatively colder seasons.

Features of Altitudinal Variation in Topside Scale Height under Varied Solar Activity

In this section, an attempt has been made to examine the topside scale height variation above h_mF_2 under different solar activity conditions using the mean H_0 and α as discussed in the previous section. A comparative assessment is also presented between the topside scale height variations derived using newly employed Hybrid reconstruction approach and the conventional Chapman approaches, as the latter remain the standard analytical formulation in most of the topside modelling studies. For this analysis, the data were binned into 30-minute LT intervals and 5-km height resolution to highlight the broad diurnal and altitudinal trends. **Figure 6** [6] illustrates the diurnal variation of topside scale height as a function of relative height $(h - h_mF_2)$, derived using the Hybrid reconstruction approach (**panels 6(a–b)**) and the Chapman method (**panels 6(c–d)**) for moderate and high solar activity conditions. In the Hybrid approach, the scale height variation at each time step was estimated from the single best-fit formulation selected based on the fitting error metrics, and the corresponding H_0 and α values were subsequently averaged within each LT bin to obtain the mean diurnal distribution. Therefore, this approach preserves the dominant diurnal and altitudinal characteristics of the topside ionosphere by statistically representing the formulation that most realistically reproduces the observed electron density structure under each geophysical condition. Here, the topside scale height is expressed as:

$$H_T(\delta) = H_0 + \alpha\,\delta \tag{1}$$

where,

$$\delta = h - h_mF_2, \qquad \alpha = \frac{\partial H}{\partial \delta} \tag{2}$$

It is evident that both the methods capture the early-morning enhancement in scale height, which is more pronounced during moderate solar activity, as well as the nighttime increase under high solar activity. However, the Hybrid reconstruction approach demonstrates the nighttime enhancement more prominently (highlighted by the black dashed box in **panel 6b**), reflecting its better ability to reproduce higher-altitude heating effects.

During the daytime hours, particularly under moderate solar activity, the Chapman method exhibit a notable reduction in scale height at higher altitudes (highlighted by white dashed box in **panel 6c**), indicating an underestimation of the actual topside temperature or scale height. This limitation arises from its assumption of a consistently negative gradient[38], which restricts its ability to reflect the gradual or near-neutral variation of scale height observed in the topside under actual conditions. On the other hand, the Hybrid reconstruction approach maintains a more realistic and continuous scale height distribution across altitude and local time, thereby avoiding such unrealistic underestimations.

To further validate these results, a full-profile ISR dataset collected at Jicamarca on 14 July 2015 was used to calculate plasma scale height for O^+ (assuming O^+ dominance in the topside) as:

$$H_{O^+} = \frac{K_\beta T_p}{m_O g} \tag{3}$$

where,

$$T_p = \frac{T_e + T_i}{2} \tag{4}$$

Here, H_{O^+} is the plasma scale height of O^+ ions, k_β ($\approx 1.38 \times 10^{-23}$ JK^{-1}) is the Boltzmann constant, T_p is the mean plasma temperature, T_e and T_i are the electron and ion temperatures respectively, m_O (≈ 16 amu; 1 amu $= 1.67 \times 10^{-27}$ kg) is the mass of the oxygen ion, and g (≈ 9.5 m s^{-2} at ionospheric altitudes) is the acceleration due to gravity.

The altitudinal variation of O^+ scale height is shown in **Figure S3** (Supplementary Material). It clearly exhibits the characteristic enhancement in the early-morning (06:00-08:00 LT) and evening-to-nighttime (16:00 - 20:00 LT) sectors. The considered day corresponds to an equinoctial period under high solar activity (average $F10.7 \approx 155$ sfu). A qualitative comparison with **Figure 6** indicates that the evening enhancement is consistently captured by both the Hybrid reconstruction approach and Chapman methods, with relatively more pronounced and continuous representation in the Hybrid case, as discussed earlier. However, the correspondence in the morning sector is comparatively less clear, reflecting inherent differences between O^+-based scale height and the effective scale height derived from electron density, as the latter represents the

contributions from multiple ion species. Further, a secondary peak can be identified in the diurnal variations of H_0 and α around 06:00 LT under high solar activity (**Figures 4** and **5**), partially complementing the observed feature. Additionally, the gradual daytime increase in plasma scale height is more consistently represented by the Hybrid reconstruction approach compared to the Chapman method. Despite these minor differences, the result show overall qualitative agreement supporting the physical reliability of the Hybrid reconstruction approach to capture key features of the diurnal and altitudinal evolution of the topside ionosphere more accurately under varying solar activity conditions. A detailed theoretical investigation of these differences is beyond the scope of the present study.

Summary and Conclusion

This study presents a comprehensive overview of performances of a newly employed Hybrid EDP reconstruction approach for reconstructing realistic vertical EDPs under diverse solar and geomagnetic conditions, using long term (2013-2024) ISR observations from JRO. This method combines the strength of the α-Chapman and semi-Epstein formulations through a time-specific, multi-metric optimization process, by reducing their individual limitations. The resulting topside parameters N_mF_2, h_mF_2, H_0 and α were analysed to access their seasonal, solar, and geomagnetic variability over electrodynamically complex equatorial region. This unique investigation highlights the advantage of a time-specific Hybrid estimation framework over conventional approaches for improving regional reconstruction accuracy of vertical EDPs. The major findings of this study are summarized below:

I. The α-Chapman function is not able to accurately reproduce the curvature of the ionospheric F-layer, particularly during daytime over the equator, with larger discrepancies near local noon. In contrast, the semi-Epstein formulation better captures the daytime characteristics but shows relatively high errors (with $nRMSE > 12\%$) during nighttime and early-morning hours.

II. The Hybrid reconstruction approach successfully reproduces actual ionospheric conditions with high reliability. In particular, the *nRMSE* remains below 5% during daytime and below 8% overall, confirming its robustness under varying solar and geomagnetic conditions.

III. The diurnal and seasonal variations in N_mF_2, h_mF_2, H_0, and α exhibit distinct temporal features. A strong correlation between h_mF_2 and H_0 is observed, whereas a weak negative correlation between N_mF_2 and α suggests that topside variability is more influenced by temperature and electrodynamical processes than by fluctuations in density.

IV. Solar activity plays a prominent role in topside ionospheric variability, while geomagnetic activity shows a comparatively negligible effect.

V. The magnitude of daytime negative α is smaller compared with earlier studies and is most evident during December Solstice, implying a gradual increase in topside scale height over the equator. These variations agree with plasma scale-height behaviour derived from full-profile ISR measurements, reinforcing the physical consistency of the Hybrid reconstruction approach.

VI. A significant nighttime enhancement in α is a unique feature observed in this study and warrants further examination at other locations. The evening peak appears earlier in June Solstice compared to December Solstice and Equinox. The sharp early-morning rise in α is more pronounced during equinox under moderate solar activity.

Future work will focus on integrating these topside observations with Ionosonde-derived bottomside profiles to develop a continuous and more precise ionospheric EDPs. Furthermore, a detailed physical investigation will be undertaken to understand the underlying mechanism driving the time-dependent Hybrid profile reconstruction approach's superior performance, particularly its ability to adaptively capture dynamic ionospheric transitions that static models like Chapman and Epstein couldn't fully resolve when used independently.

Methods

Primary Data Source: Jicamarca ISR EDPs

The primary dataset used in this study comprises electron density profiles (EDPs) obtained from ISR measurements at the Jicamarca Radio Observatory (JRO). The JRO-ISR serves as the centrepiece of a suite of advanced radio and optical remote-sensing instruments designed for equatorial ionospheric research. This system operates at 50 MHz, featuring megawatt-class transmitters and a 300 m $\times$ 300 m modular antenna array, possessing the largest power–aperture product in the VHF band worldwide[40]. The radar employs the traditional double-pulse Faraday rotation technique to retrieve altitude-resolved plasma parameters by

measuring incoherent backscattered signals from free electrons[57].The derived parameters typically cover an altitude range from $\sim$ 90 km to $\sim$ 600–800 km, depending on the prevailing ionospheric conditions. Furthermore, for full-profile composition analysis extending up to $\sim$ 1400–1500 km, a special long-pulse mode is incorporated along with the standard configuration to enhance sensitivity to topside measurements[13]. The EDPs used in this study were accessed from the publicly available, quality-controlled CEDAR Madrigal database (https://cedar.openmadrigal.org/). All available electron density data from both normal and full-profile mode measurements during 2013–2024 were utilized in the analysis; however, no density data were available for the year 2016.

In addition, to study the influence of solar and geomagnetic activity on the topside parameters, daily average values of the ***F10.7* solar flux** and the **K_p index** were also incorporated into the analysis. These indices were obtained from the NASA OMNIWeb database (https://omniweb.gsfc.nasa.gov/).

Hybrid Reconstruction Approach for Extracting the Topside Scale Height and Its Linear Gradient

The Hybrid reconstruction approach employed in this study is designed to extract key topside ionospheric parameters, including the scale height at F_2 peak (H_0) and its linear altitudinal gradient (α), from ISR derived EDPs in a more physically consistent manner. This approach combines analytical modelling, iterative least square fitting, and selection of best-fit topside parameters based on quantitative error metrics. For easy understanding of the readers, the complete workflow is summarized in the flow chart shown in **Figure 7** [7] and described as follows.

(a) Initial Processing of EDP Data

All available ISR-measured EDPs were manually inspected to remove incomplete or highly unstable profiles. Only data above 200 km were retained, as the analysis primarily focuses on the F-region, and measurements at lower altitudes often contain unrealistic values due to larger measurement uncertainties or E-region disturbances. Profiles exhibiting unrealistic electron densities (negative values or densities exceeding $10^{13}\,\mathrm{m}^{-3}$), or those lacking a well-defined h_mF_2 peak, were excluded. Each accepted profile was then interpolated to a uniform 5 km vertical grid to enhance the identification of peak parameters and to facilitate consistent model fitting, as the original ISR altitude resolution is typically $\sim$ 10–15 km. For each valid profile, the observed values of N_mF_2 and h_mF_2 were initially extracted from the interpolated ISR profiles as a reference for further analysis. However, these directly identified peak parameters are subjected to uncertainties associated with the sparse altitude resolution and interpolation of ISR measurements.

(b) Analytical Model Formulation

The F-region EDP was represented using two standard analytical formulations:

I. α-Chapman Function: This is a widely used analytical representation to describe the electron density distribution of the ionosphere[58], especially around the F-region.

$$N_e(h) = N_mF_2 \exp\left[\frac{1}{2}\left(1 - z - exp(-z)\right)\right] \tag{5}$$

II. Semi-Epstein Function: This empirical model provides a smoother transition between the bottomside and topside regions, allowing greater flexibility in fitting observed profiles[28].

$$N_e(h) = 4N_mF_2 \frac{\exp(z)}{(1+\exp(z))^2} \tag{6}$$

For both formulations the variable z is defined as:

$$z = \frac{h - h_mF_2}{H_0 + \alpha\,(h - h_mF_2)} \tag{7}$$

where, for the bottomside ionosphere, $\alpha = 0$. Here, $N_e(h)$ denotes the electron density at height h; N_mF_2 and h_mF_2 represent F_2 peak density and height respectively; H_0 is the scale height at the peak; and α is the linear gradient of the topside scale height.

(c) Hybrid Fitting and Parameter Extraction

The steps involved in the Hybrid profile fitting procedure are as follows:

I. For each considered EDP, both α-Chapman and Semi-Epstein formulations were independently fitted to the observed $N_e(h)$ using nonlinear least-squares optimization, by treating the N_mF_2, h_mF_2, h_0, and α as free parameters during the fitting process. Although, the observed ISR-derived N_mF_2 and h_mF_2 were used as initial reference values, they were not strictly constrained during the optimization, since it is found that, fixing these parameters degraded the overall profile reconstruction by preferentially biasing the fitting towards the peak region. Consequently, the fitted peak parameters may slightly differ from the directly observed ISR profiles and between formulations, reflecting their inherent differences in representing the observed profile shape.

II. The H_0 was then iteratively varied between 10 and 150 km to obtain the best-fit F-layer EDP for both formulations.

III. For the obtained best-fit H_0, the gradient α was varied between -1 and 1 km^{-1} to achieve the optimum topside fit.

IV. The error metrics for each fitted profile were computed as follows:

1. **Root Mean Square Error (RMSE):**

$$RMSE = \sqrt{\frac{1}{n}\sum_{i=1}^{n}\left(N_{e,\mathrm{obs}}(h_i) - N_{e,\mathrm{fit}}(h_i)\right)^2} \tag{8}$$

2. **Normalized RMSE (nRMSE):**

$$nRMSE = \frac{RMSE}{N_mF_{2,(\mathrm{observed})}} \times 100\% \tag{9}$$

3. **Difference in F_2 Peak Height:**

$$\Delta h_mF_2 = \frac{\left|h_mF_2^{\mathrm{observed}} - h_mF_2^{\mathrm{fitted}}\right|}{h_mF_2^{\mathrm{observed}}} \times 100\% \tag{10}$$

V. A composite error index (CEI) was then computed to quantitatively evaluate the overall fitting accuracy of each model:

$$\mathrm{CEI} = \frac{w_1(RMSE) + w_2(nRMSE) + w_3(\Delta h_mF_2)}{3} \tag{11}$$

where w_1, w_2, and w_3 are weights assigned to each error metric. In principle, the optimal values of these weights can be determined by testing different combinations, depending on the relative importance given to each metric in evaluating the reconstruction performance. Tests with combination of different weights showed no significant change in the relative model performance. Eventually, an equal weight of 1 was assigned to each of them. The conceptualization of this multi-metric fitting error index was inspired by various validation strategies adopted in previous ionospheric model evaluation studies[22,38,44], emphasizing the importance of combining multiple statistical indicators for determining reconstruction accuracy.

VI. Finally, for each observation the model yielding the lowest CEI was dynamically selected as the best-fit Hybrid formulation for reconstruction of EDPs. The corresponding values of N_mF_2, h_mF_2, H_0 and α from the selected best-fit formulation were retained as effective Hybrid topside parameters for subsequent statistical analysis.

It is important to note that, no altitude range was excluded from the fitting procedure, including the region immediately above h_mF_2, where the Chapman function is known to exhibit mathematical limitations[4] in the scale height representation. In several earlier studies dedicated specifically to topside scale height estimation, the region above h_mF_2 to approximately h_mF_2 + 50 km is generally excluded during calculation of scale height and its gradient. A similar approach was adopted in earlier studies based on COSMIC RO profiles[31,33]. Such approaches generally assume that the topside profile already follows a specific analytical formulation, from which the corresponding scale height variation is subsequently estimated. However, the objective of the present study is fundamentally different. Here, the scale height and its gradient are not directly calculated from the observed topside profile. Instead, they are iteratively varied within both analytical formulations to determine which combination best reproduces the complete observed vertical electron density distribution. The final selection of the optimum formulation is then performed using quantitative fitting error metrics. Hence, retaining the full profile, including the transition region near to F_2 peak, is essential for a comprehensive assessment of each formulation in reproducing the overall F-region curvature, which is essential for realistic ionospheric modelling.

(d) Final Quality Control and Filtering

All invalid, noisy, and anomalous profiles were removed through a set of strict quality-control filters to ensure the reliability of the retrieved parameters. The final dataset includes only profiles satisfying the following selection criteria:

I. $10^9\ \mathrm{m}^{-3} \leq N_m F_2 \leq 10^{13}\ \mathrm{m}^{-3}$

II. $200\ \mathrm{km} \leq h_m F_2 \leq 500\ \mathrm{km}$

III. $10\ \mathrm{km} \leq H_0 \leq 150\ \mathrm{km}$

IV. $-1 < \alpha < 1$

V. $nRMSE < 15\%$

A total of 243 days of electron density observations from 2013–2024 were considered in this study, corresponding to over 20,000 individual profiles. After applying the above filtering criteria, 19,201 high-quality profiles were retained for further analysis.

References

1. Rishbeth, H. & Garriott, O. K. *Introduction to Ionospheric Physics* (1969).
2. Rishbeth, H. The equatorial f-layer: progress and puzzles. *Annales Geophys.* **18**, 730–739, DOI: 10.1007/s00585-000-0730-6 (2000).
3. Sripathi, S. *et al.* Characteristics of the equatorial plasma drifts as obtained by using canadian doppler ionosonde over southern tip of india. *J. Geophys. Res. Space Phys.* **121**, 8103–8120, DOI: 10.1002/2016JA023088 (2016).
4. Huang, X. & Reinisch, B. W. Vertical electron content from ionograms in real time. *Radio Sci.* **36**, 335–342, DOI: 10.1029/1999RS002409 (2001).
5. Bilitza, D. Evaluation of the iri-2007 model options for the topside electron density. *Adv. Space Res.* **44**, 701–706, DOI: 10.1016/j.asr.2009.04.036 (2009).
6. Sinha, H. S. S. & Raizada, S. First in situ measurement of electric field fluctuations during strong spread f in the indian zone. *Annales Geophys.* **18**, 523–531, DOI: 10.1007/s00585-000-0523-y (2000).
7. Friis-Christensen, E., Lühr, H. & Hulot, G. Swarm: A constellation to study the earth's magnetic field. *Earth, Planets Space* **58**, 351–358, DOI: 10.1186/BF03351933 (2006).
8. Schreiter, L. *et al.* Topside ionosphere sounding from the champ, grace, and grace-fo missions. *Radio Sci.* **58**, DOI: 10.1029/2022RS007552 (2023).
9. Sripathi, S. Cosmic observations of ionospheric density profiles over indian region: Ionospheric conditions during extremely low solar activity period. *Indian J. Radio & Space Phys.* **41** (2012).
10. Schreiner, W. S. *et al.* Cosmic-2 radio occultation constellation: First results. *Geophys. Res. Lett.* **47**, DOI: 10.1029/2019GL086841 (2020).
11. Liu, L. *et al.* Variations of topside ionospheric scale heights over millstone hill during the 30-day incoherent scatter radar experiment. *Annales Geophys.* **25** (2019).
12. Luan, X. *et al.* A study of the shape of topside electron density profile derived from incoherent scatter radar measurements over arecibo and millstone hill. *Radio Sci.* **41**, DOI: 10.1029/2005RS003367 (2006).
13. Hysell, D. L., Milla, M. A., Rodrigues, F. S., Varney, R. H. & Huba, J. D. Topside equatorial ionospheric density, temperature, and composition under equinox, low solar flux conditions. *J. Geophys. Res. Space Phys.* **120**, 3899–3912, DOI: 10.1002/2015JA021168 (2015).
14. Derghazarian, S., Hysell, D. L. & Varney, R. H. Topside measurements at jicamarca during the 2019–2020 deep solar minimum. *J. Geophys. Res. Space Phys.* **126**, DOI: 10.1029/2021JA029695 (2021).
15. Hysell, D. L., Chau, J. L. & Huba, J. D. Topside measurements at jicamarca during solar minimum. *Annales Geophys.* **27**, 427–2009 (2009).
16. Bilitza, D. *et al.* The international reference ionosphere model: A review and description of an ionospheric benchmark. *Rev. Geophys.* **60**, DOI: 10.1029/2022RG000792 (2022).

506 **17.** Nava, B., Coïsson, P. & Radicella, S. M. A new version of the nequick ionosphere electron density model. *J. Atmospheric*
507 *Solar-Terrestrial Phys.* **70**, 1856–1862, DOI: 10.1016/j.jastp.2008.01.015 (2008).

508 **18.** Huba, J. D., Joyce, G. & Fedder, J. A. Sami2 is another model of the ionosphere (sami2): A new low-latitude ionosphere
509 model. *J. Geophys. Res. Space Phys.* **105**, 23035–23053, DOI: 10.1029/2000JA000035 (2000).

510 **19.** Coïsson, P., Radicella, S. M., Leitinger, R. & Nava, B. Topside electron density in iri and nequick: Features and limitations.
511 *Adv. Space Res.* **37**, 937–942, DOI: 10.1016/j.asr.2005.09.015 (2006).

512 **20.** Lee, C.-C. & Reinisch, B. W. Quiet-condition hmf2, nmf2, and b0 variations at jicamarca and comparison with iri-2001
513 during solar maximum. *J. Atmospheric Solar-Terrestrial Phys.* **68**, 2138–2146, DOI: 10.1016/j.jastp.2006.07.007 (2006).

514 **21.** Pignalberi, A. *et al.* Climatological study of the ion temperature in the ionosphere as recorded by millstone hill incoherent
515 scatter radar and comparison with the iri model. *Adv. Space Res.* **68**, 2186–2203, DOI: 10.1016/j.asr.2020.10.025 (2021).

516 **22.** Iluore, K., Lu, J., Okeke, F. & Keyston, O. Performance of nequick-2 and iri-plas 2017 models during solar maximum
517 years in 2013-2014 over equatorial and low latitude regions. *Universe* **8**, DOI: 10.3390/universe8020125 (2022).

518 **23.** Barad, R. K., Sripathi, S., Singh, R., Gayathri, B. & Abadi, P. Observations and modeling investigations of ionospheric
519 response to 23–24 april 2023, g4-class geomagnetic storm over indian sector. *Space Weather.* **23**, DOI: 10.1029/
520 2024SW004253 (2025).

521 **24.** Stankov, S. M. *et al.* A new method for reconstruction of the vertical electron density distribution in the upper ionosphere
522 and plasmasphere. *J. Geophys. Res. Space Phys.* **108**, DOI: 10.1029/2002JA009570 (2003).

523 **25.** Tulasi Ram, S., Su, S. Y., Liu, C. H., Reinisch, B. W. & McKinnell, L. A. Topside ionospheric effective scale heights (ht)
524 derived with rocsat-1 and ground-based ionosonde observations at equatorial and midlatitude stations. *J. Geophys. Res.*
525 *Space Phys.* **114**, DOI: 10.1029/2009JA014485 (2009).

526 **26.** Venkatesh, K., Rama Rao, P. V. S., Saranya, P. L., Prasad, D. S. V. V. D. & Niranjan, K. Vertical electron density and
527 topside effective scale height (ht) variations over the indian equatorial and low latitude stations. *Annales Geophys.* **29**,
528 1861–1872, DOI: 10.5194/angeo-29-1861-2011 (2011).

529 **27.** Olivares-Pulido, G., Hernández-Pajares, M., Aragón-Àngel, A. & Garcia-Rigo, A. A linear scale height chapman model
530 supported by gnss occultation measurements. *J. Geophys. Res. Space Phys.* **121**, 7932–7940, DOI: 10.1002/2016JA022337
531 (2016).

532 **28.** Radicella, S. M. & Leitinger, R. The evolution of the dgr approach to model electron density profiles. *Adv. Space Res.* **27**,
533 35–40, DOI: 10.1016/S0273-1177(00)00138-1 (2001).

534 **29.** Leitinger, R., Zhang, M. L. & Radicella, S. M. An improved bottomside for the ionospheric electron density model nequick.
535 *Annals Geophys.* **48** (2005).

536 **30.** Venkatesh, K., Pallamraju, D., Pant, T. K. & Suryawanshi, P. Parametric dependence of topside ionospheric empirical scale
537 height and electron density profiles in nequick2 model over the equatorial and low latitudes and its consequences on the
538 estimation of tec. *J. Geophys. Res. Space Phys.* **128**, DOI: 10.1029/2023JA031335 (2023).

539 **31.** Siba Kiran Guru, K., Sripathi, S. & Barad, R. K. A novel approach of reconstructing the topside ionosphere using
540 ionosonde and cosmic scale height gradients: Validation with swarm measurements. *Radio Sci.* **60**, e2025RS008356, DOI:
541 10.1029/2025RS008356 (2025).

542 **32.** Verhulst, T. & Stankov, S. M. Ionospheric specification with analytical profilers: Evidences of non-chapman electron
543 density distribution in the upper ionosphere. *Adv. Space Res.* **55**, 2058–2069, DOI: 10.1016/j.asr.2014.10.017 (2015).

544 **33.** Pignalberi, A., Pezzopane, M., Nava, B. & Coïsson, P. On the link between the topside ionospheric effective scale height
545 and the plasma ambipolar diffusion, theory and preliminary results. *Sci. Reports* **10**, DOI: 10.1038/s41598-020-73886-4
546 (2020).

547 **34.** Liu, L. *et al.* Deriving the effective scale height in the topside ionosphere based on ionosonde and satellite in situ
548 observations. *J. Geophys. Res. Space Phys.* **119**, 8472–8482, DOI: 10.1002/2014JA020505 (2014).

549 **35.** Pignalberi, A., Pezzopane, M. & Rizzi, R. Modeling the lower part of the topside ionospheric vertical electron density
550 profile over the european region by means of swarm satellites data and iri up method. *Space Weather.* **16**, 304–320, DOI:
551 10.1002/2017SW001790 (2018).

552 **36.** Hernández-Pajares, M. *et al.* Electron density extrapolation above f2 peak by the linear vary-chap model supporting
553 new global navigation satellite systems-leo occultation missions. *J. Geophys. Res. Space Phys.* **122**, 9003–9014, DOI:
554 10.1002/2017JA023876 (2017).

37. dos Santos Prol, F., Themens, D. R., Hernández-Pajares, M., de Oliveira Camargo, P. & de Assis Honorato Muella, M. T. Linear vary-chap topside electron density model with topside sounder and radio-occultation data. *Surv. Geophys.* **40**, 277–293, DOI: 10.1007/s10712-019-09521-3 (2019).

38. Gao, S. *et al.* Altitudinal variation of o+ scale height at the equatorial topside ionosphere. *J. Geophys. Res. Space Phys.* **129**, DOI: 10.1029/2024JA033033 (2024).

39. Prol, F. S., Smirnov, A. G., Hoque, M. M. & Shprits, Y. Y. Combined model of topside ionosphere and plasmasphere derived from radio-occultation and van allen probes data. *Sci. Reports* **12**, 1–11, DOI: 10.1038/s41598-022-13302-1 (2022).

40. Woodman, R. F., Farley, D. T., Balsley, B. B. & Milla, M. A. The early history of the jicamarca radio observatory and the incoherent scatter technique. *Hist. Geo- Space Sci.* **10**, 245–266, DOI: 10.5194/hgss-10-245-2019 (2019).

41. Huang, C., Zhang, Y., Wang, W., Lin, D. & Wu, Q. Behaviors of ionospheric topside ion density, ion temperature, and electron temperature during the 20 november 2003 superstorm. *J. Geophys. Res. Space Phys.* **127**, DOI: 10.1029/2022JA030468 (2022).

42. Fonda, C., Coïsson, P., Nava, B. & Radicella, S. M. Comparison of analytical functions used to describe topside electron density profiles with satellite data. *Annals Geophys.* **48**, DOI: 10.4401/ag-3213 (2005).

43. Verhulst, T. & Stankov, S. M. Evaluation of ionospheric profilers using topside sounding data. *Radio Sci.* **49**, 181–195, DOI: 10.1002/2013RS005263 (2014).

44. Pignalberi, A. *et al.* On the electron temperature in the topside ionosphere as seen by swarm satellites, incoherent scatter radars, and the international reference ionosphere model. *Remote. Sens.* **13**, 4077, DOI: 10.3390/rs13204077 (2021).

45. Balan, N., Bailey, G. J., Nair, R. B. & Titheridge, J. E. Nighttime enhancements in ionospheric electron content in the northern and southern hemispheres. *J. Atmospheric Terr. Phys.* **56**, 67–79, DOI: 10.1016/0021-9169(94)90177-5 (1994).

46. Wang, Y. *et al.* Ionospheric nighttime enhancements in the equatorial region as revealed by the beidou geostationary tec observations. *J. Geophys. Res. Space Phys.* **127**, DOI: 10.1029/2022JA030483 (2022).

47. Liu, L. *et al.* Structure of post-midnight enhancements in electron density at the low latitude f-layer ionosphere. *J. Geophys. Res. Space Phys.* **128**, DOI: 10.1029/2023JA031376 (2023).

48. Fejer, B. G., Jensen, J. W. & Su, S. Seasonal and longitudinal dependence of equatorial disturbance vertical plasma drifts. *Geophys. Res. Lett.* **35**, DOI: 10.1029/2008GL035584 (2008).

49. Yang, C., Zhao, B., Zhu, J., Yue, X. & Wan, W. An investigation of ionospheric upper transition height variations at low and equatorial latitudes deduced from combined cosmic and c/nofs measurements. *Adv. Space Res.* **60**, 1617–1628, DOI: 10.1016/j.asr.2016.11.024 (2017).

50. Vaishnav, R. *et al.* Study of the upper transition height using isr observations and iri predictions over arecibo. *Adv. Space Res.* **68**, 2177–2185, DOI: 10.1016/j.asr.2020.10.010 (2021).

51. Prol, F. d. S., Hernández-Pajares, M., de Oliveira Camargo, P. & Muella, M. T. d. A. H. Spatial and temporal features of the topside ionospheric electron density by a new model based on gps radio occultation data. *J. Geophys. Res. Space Phys.* **123**, 2104–2115, DOI: 10.1002/2017JA024936 (2018).

52. Smirnov, A. *et al.* A novel neural network model of earth's topside ionosphere. *Sci. Reports* **13**, 1–11, DOI: 10.1038/s41598-023-28034-z (2023).

53. Pignalberi, A., Pezzopane, M. & Nava, B. Optimizing the nequick topside scale height parameters through cosmic/formosat-3 radio occultation data. *IEEE Geosci. Remote. Sens. Lett.* **19**, DOI: 10.1109/LGRS.2021.3096657 (2022).

54. Stolle, C., Liu, H., Truhlík, V., Lühr, H. & Richards, P. G. Solar flux variation of the electron temperature morning overshoot in the equatorial f region. *J. Geophys. Res. Space Phys.* **116**, DOI: 10.1029/2010JA016235 (2011).

55. Yang, T. *et al.* Morning overshoot of electron temperature as observed by the swarm constellation and the international space station. *J. Geophys. Res. Space Phys.* **125**, DOI: 10.1029/2019ja027299 (2020).

56. Fejer, B. G., Hysell, D. L. & Navarro, L. A. Anomalous electron temperature increases in the evening equatorial ionosphere. *J. Geophys. Res. Space Phys.* **126**, DOI: 10.1029/2020ja028728 (2021).

57. Farley, D. T. Incoherent scatter correlation function measurements. *Radio Sci.* **4**, 935–953, DOI: 10.1029/RS004i010p00935 (1969).

58. Chapman, S. The absorption and dissociative or ionizing effect of monochromatic radiation in an atmosphere on a rotating earth. *Proc. Phys. Soc.* **43**, 26–45, DOI: 10.1088/0959-5309/43/1/305 (1931).

Acknowledgements

We sincerely thank the Indian Institute of Geomagnetism (IIG), Navi Mumbai for providing necessary support in carrying out this work through the in-house project DECA (Dynamical and Electrodynamical Coupling of Atmosphere-Ionosphere). The corresponding author, K.S.K. Guru, specifically acknowledge the Jicamarca Radio Observatory (JRO) and the Geophysical Institute of Peru (IGP) for providing the exposure to an international research environment, and necessary facilities to conduct this study under the JRO International Research Experience Programme (JIREP 2025). The financial support from Ciencia International (CI) and the U.S. National Science Foundation (NSF) for funding this program is also sincerely acknowledged. Finally, the corresponding author extends his heartfelt thanks to the entire JRO technical and administrative team for operating and maintaining the ISR system and for collecting the high-quality data that were instrumental in successfully completing this work.

Author Contributions

K.S.K.G.: Conceptualization, methodology, software, validation, formal analysis, writing-original draft. ***S.S.***: Supervision, writing-review & editing, investigation, validation. ***R.S.***: Methodology, writing-review & editing, supervision, investigation. ***R.K.B.***: Writing-review & editing, validation. ***D.S.***: Data acquisition, writing-review & editing, investigation, validation. ***A.P.D.***: Writing-review & editing, investigation, validation. All authors reviewed and agreed to the present version of manuscript.

Competing Interest Statement

The authors declare no competing interest.

Funding Declaration

The authors declare that this research did not receive any external funding.

Data Availability Statement

The raw electron density data from the Jicamarca Incoherent Scatter Radar (ISR-JRO) are available through the CEDAR Madrigal database at https://cedar.openmadrigal.org/.These data may be used with permission from the Principal Investigator (PI) of ISR-JRO, in accordance with Jicamarca Radio Observatory (JRO) data-sharing policies. The processed electron density, electron temperature, ion temperature, and ion concentration data that support findings of this study are available from the corresponding author upon reasonable request, subject to JRO and Indian institute of Geomagnetism (IIG) data-sharing norms. Solar and geomagnetic indices used in this study were obtained from the NASA OMNIWeb database at https://omniweb.gsfc.nasa.gov/.

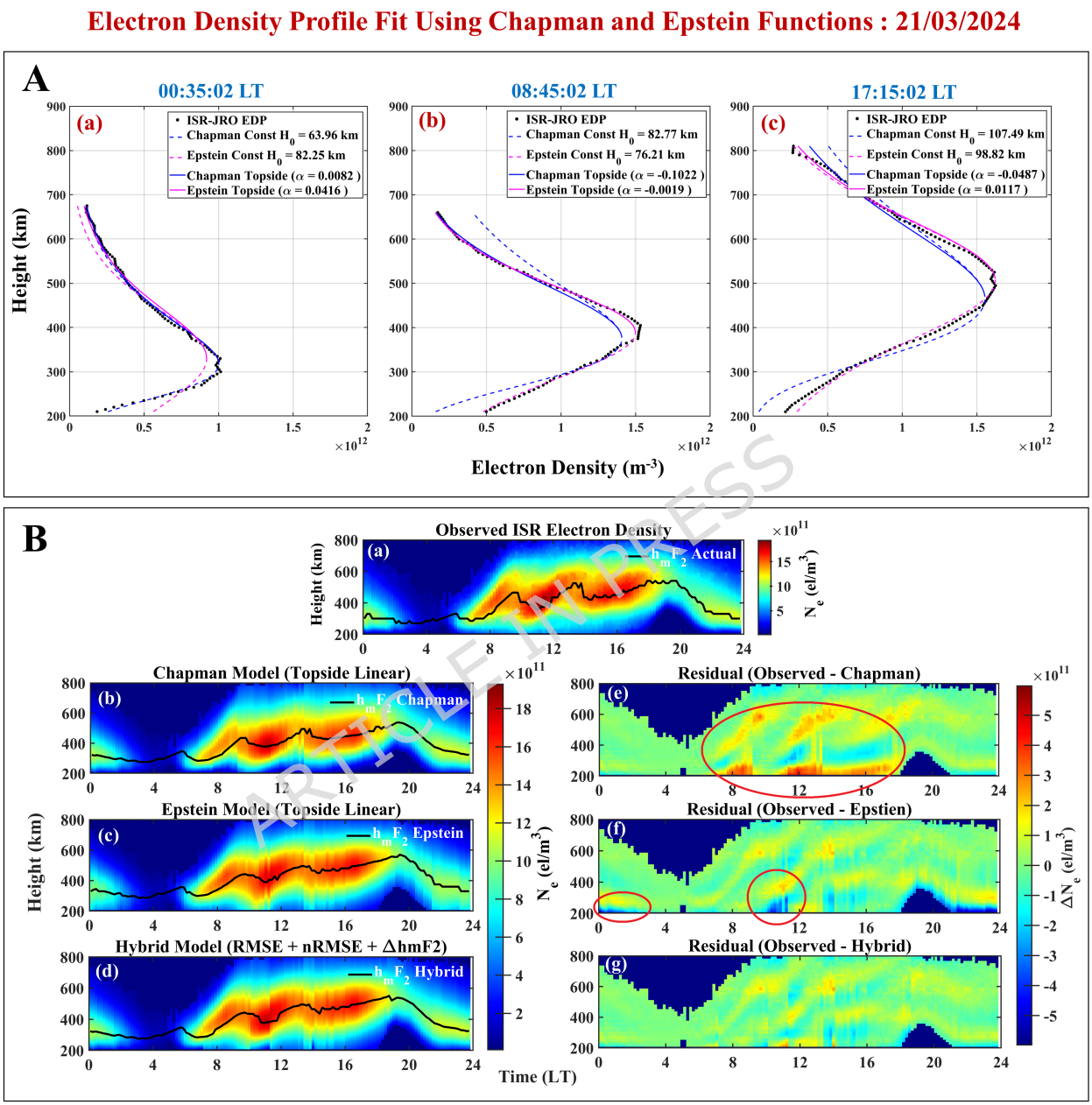

Figure 1. ISR electron density profile fitting Using Chapman and Epstein Functions for a typical day (21 March 2024). **Panel (A: a-c)** shows the least-square fitting of actual electron density profiles with empirical formulations for three selected time intervals. **Panel (B: a-c)** presents the Range-Time-Density (or Residual) plots for the same day, comparing the relative performance of Hybrid reconstruction approach.

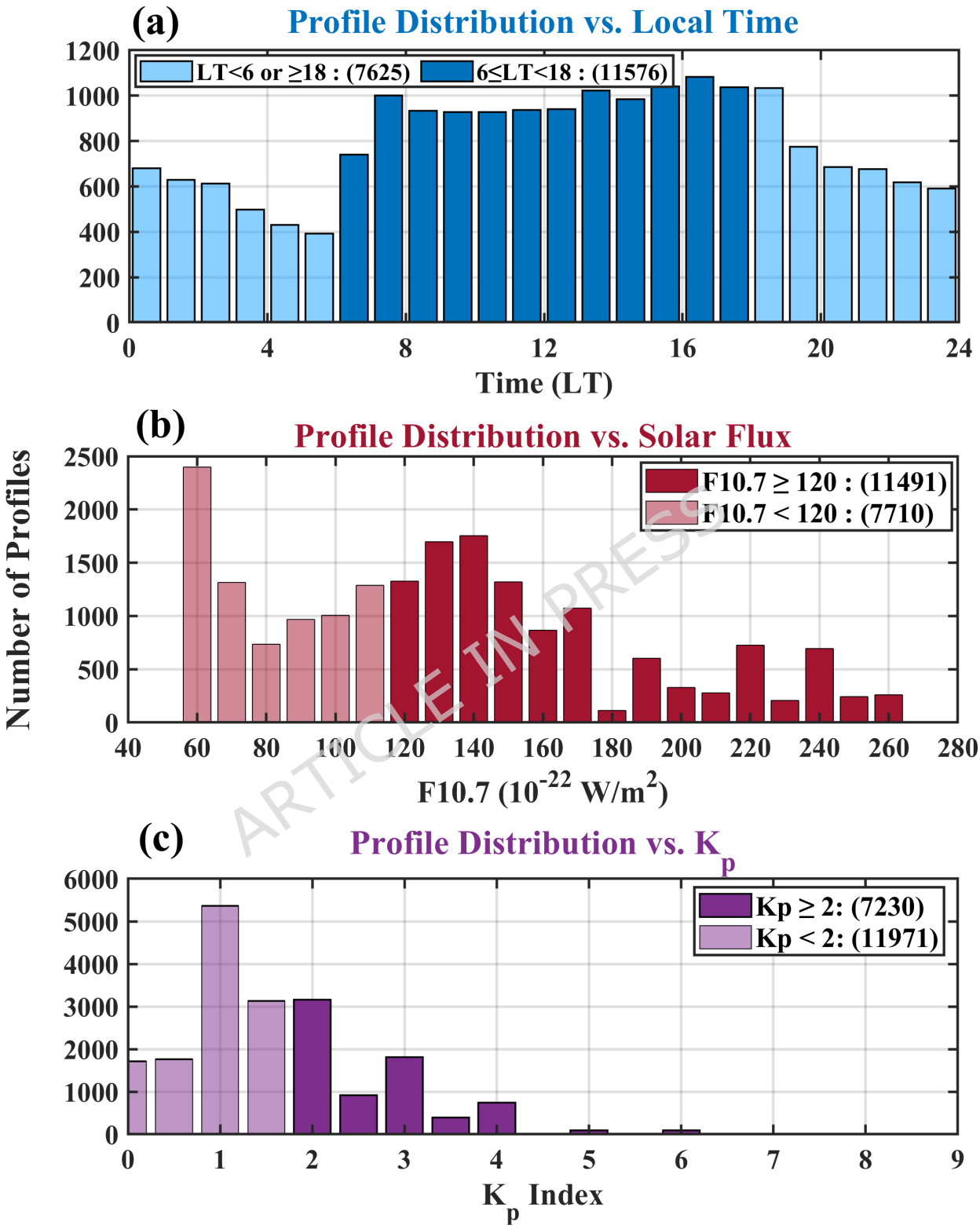

Figure 2. Distribution statistics of considered ISR electron density profiles with respect to **(a)** Local Time, **(b)** *F10.7* Solar Flux, and **(c)** K_p Index. The corresponding number of profiles for each condition is indicated in the legends.

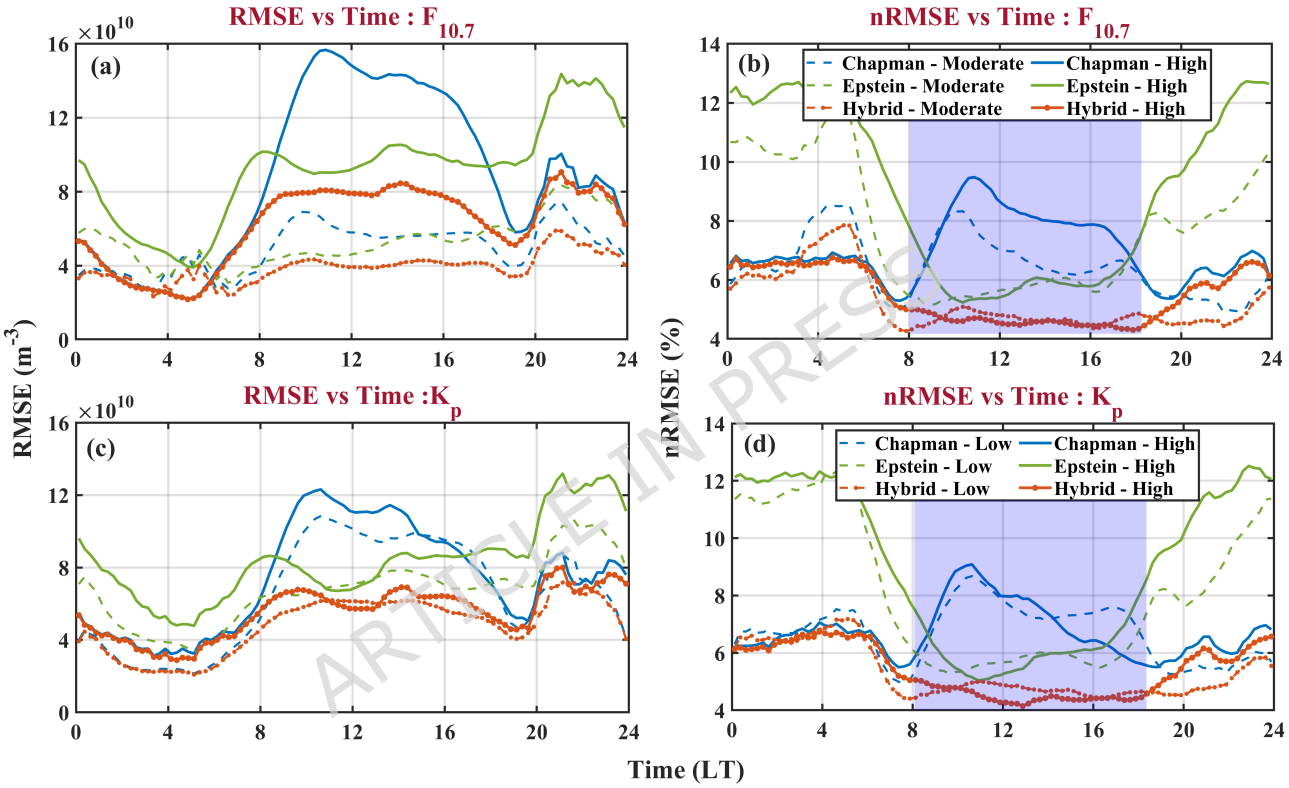

Figure 3. Error analysis demonstrating the improved performance of the Hybrid reconstruction approach. **Panels (a)** and **(b)** show variation of *RMSE* in density with respect to *F10.7* solar flux and K_p index, respectively. Similarly, **Panels (c)** and **(d)** present the corresponding *nRMSE* in density variation with respect to *F10.7* solar flux and K_p index.

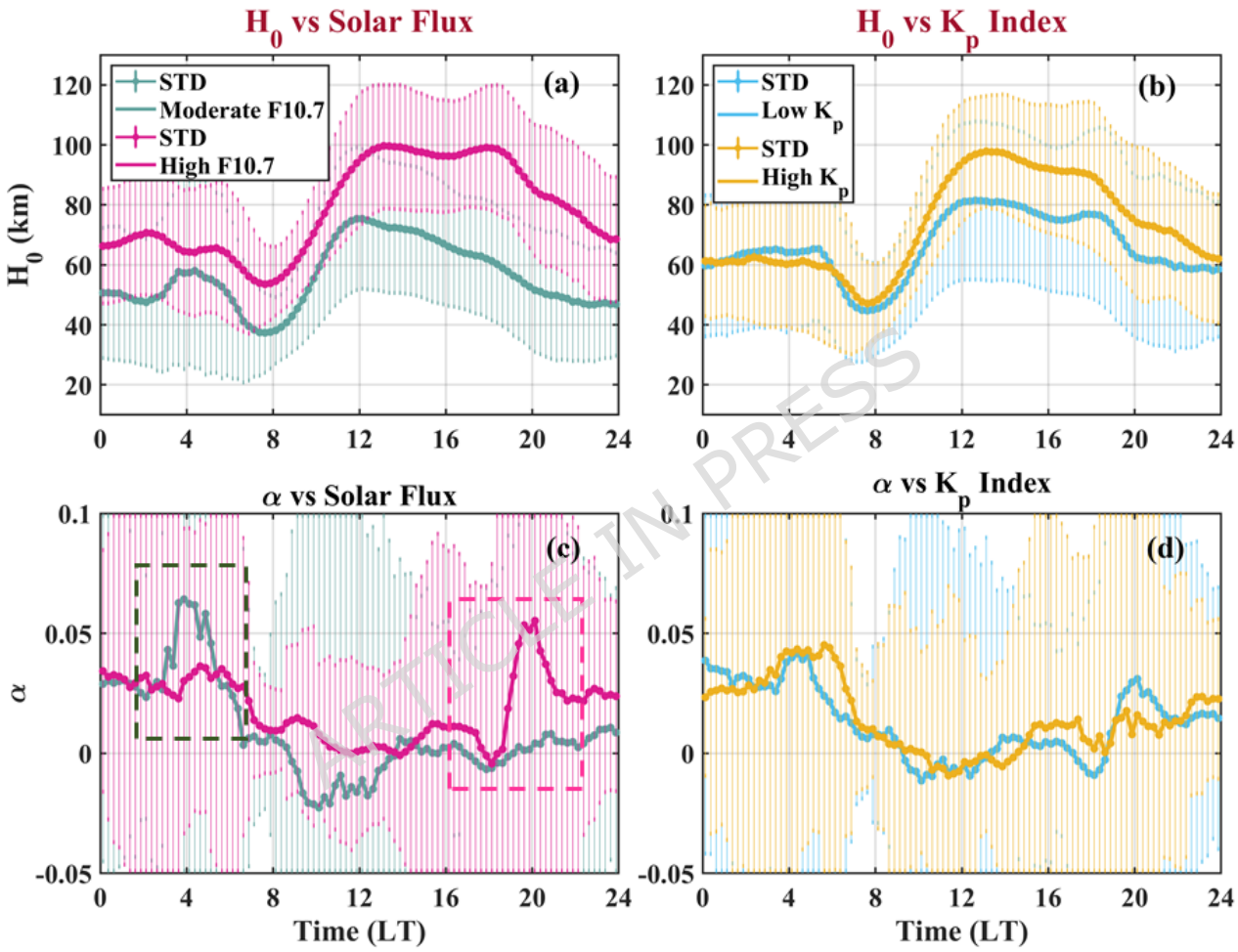

Figure 4. Diurnal variation of H_0 and α under varied solar and geomagnetic conditions. **Panels (a)** and **(b)** show the variation of H_0 with respect to *F10.7* solar flux and K_p index, respectively. Similarly, **Panels (c)** and **(d)** present the corresponding α variation with respect to *F10.7* solar flux and K_p index.

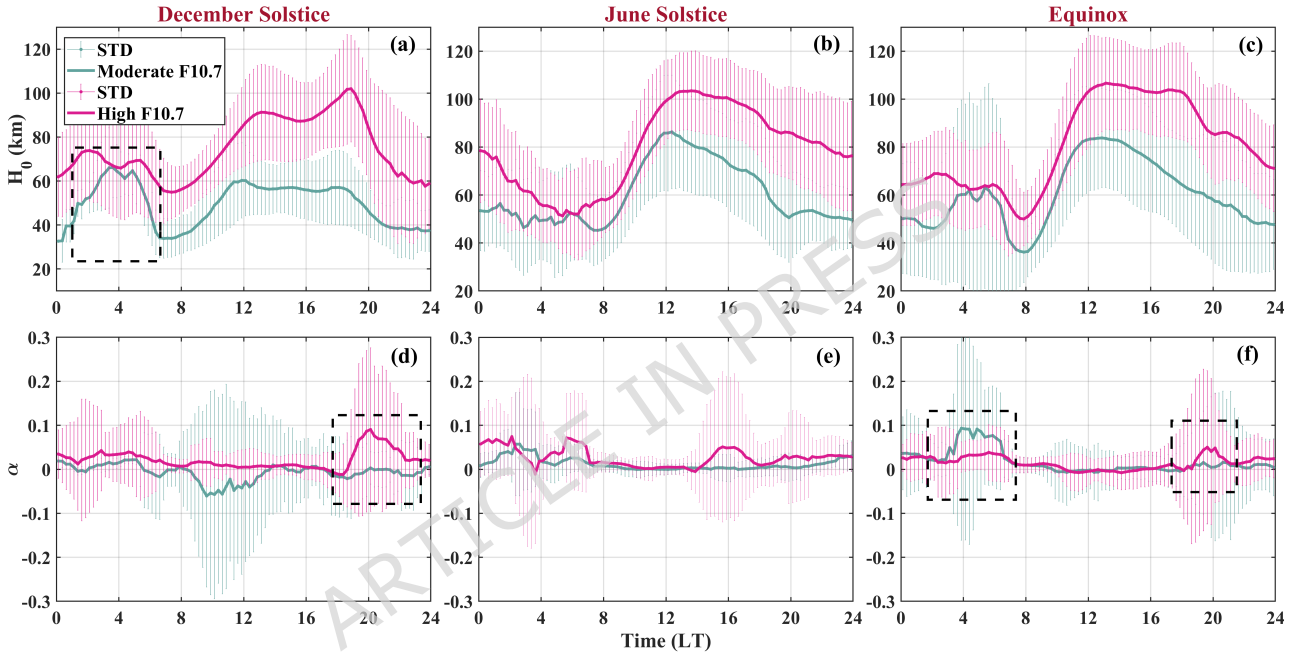

Figure 5. Seasonal diurnal variation of H_0 and α under varied solar and geomagnetic conditions. **Panels (a-c)** show the variation of H_0, and **Panels (d-f)** present the corresponding variation of α for **December Solstice (southern summer)**, **June Solstice (southern winter)** and **Equinox** seasons, respectively.

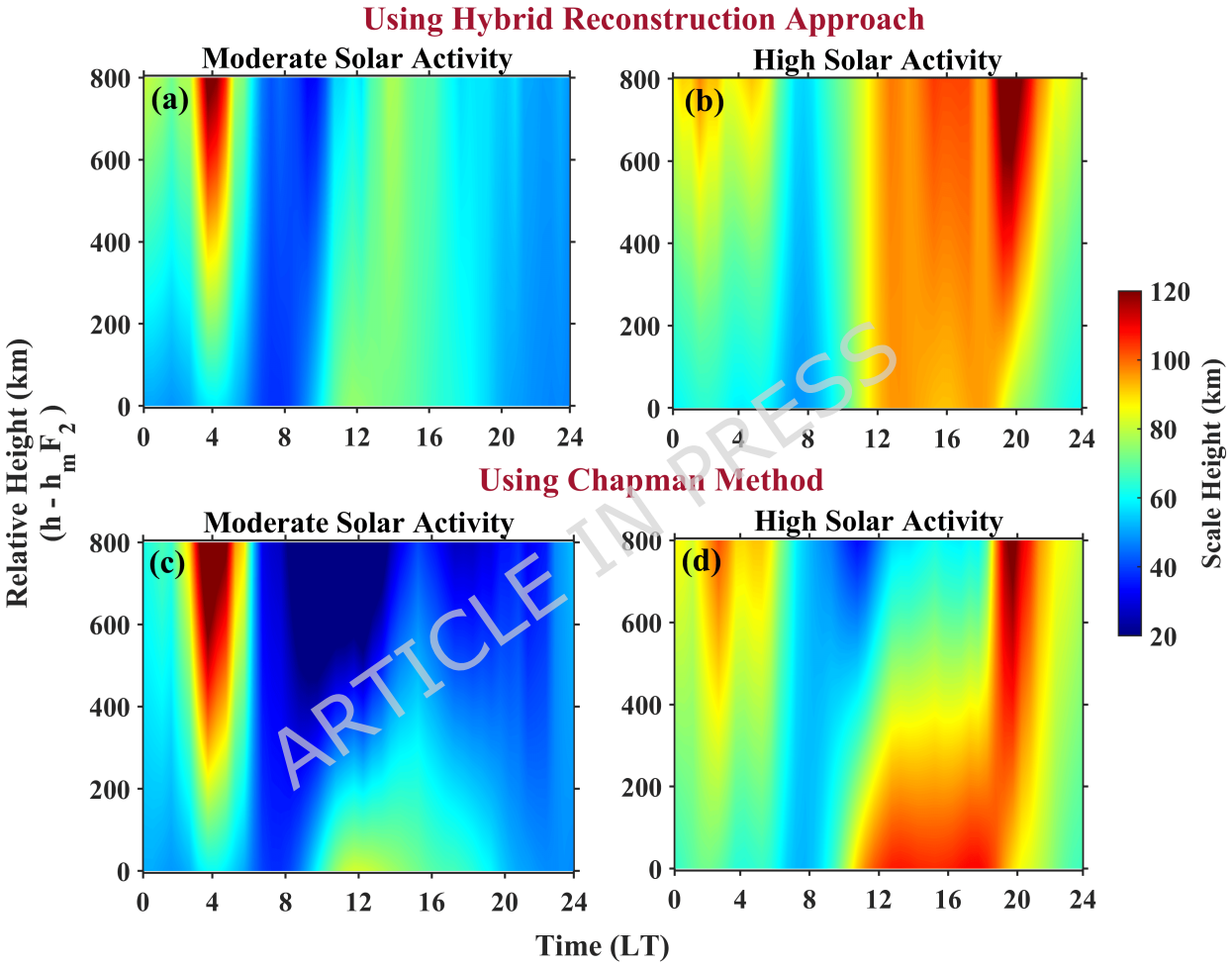

Figure 6. Topside scale height variation under different solar activity conditions. **Panels (a)** and **(b)** corresponds to *Hybrid reconstruction approach*, while **Panels (c)** and **(d)** represent the same derived using Chapman function.

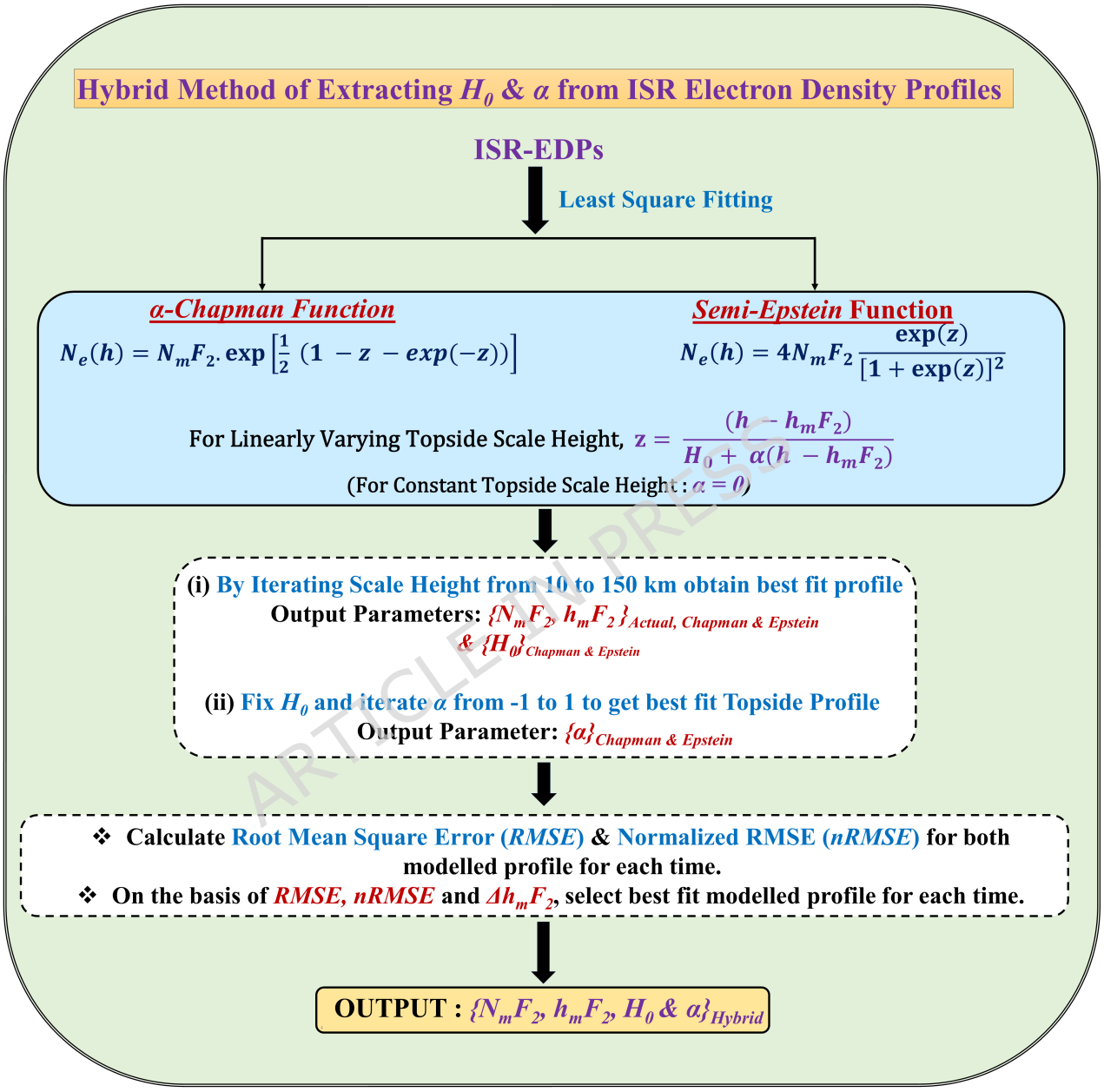

Figure 7. Flow chart illustrating the sequential steps involved in the Hybrid reconstruction approach for extracting the topside parameters H_0 and α.